Magnetotransport Experiments on Fully Metallic Superconducting Dayem-Bridge Field-Effect Transistors

Federico Paolucci,[1,2,*] Giorgio De Simoni,[2] Paolo Solinas,[3] Elia Strambini,[2] Nadia Ligato,[2] Pauli Virtanen,[2] Alessandro Braggio,[2] and Francesco Giazotto[2]

[1] *INFN Sezione di Pisa, Largo Bruno Pontecorvo 3, 56127 Pisa, Italy*

[2] *CNR Instituto Nanoscienze and Scuola Normale Superiore, NEST, Piazza San Silvestro 12, 56127 Pisa, Italy*

[3] *CNR SPIN, Via Dodecaneso 33, 16146 Genoa, Italy*

(Received 31 July 2018; revised manuscript received 17 December 2018; published 25 February 2019)

In the last 60 years conventional solid and electrolyte gating has allowed sizable modulations of the surface carrier concentration in metallic superconductors, resulting in tuning of their conductivity and change of their critical temperature. Recent conventional gating experiments on superconducting metal nanostructures showed full suppression of the critical current without variation of the normal-state resistance and the critical temperature. These results still lack a microscopic explanation. In this article, we describe a complete set of gating experiments on Ti-based superconducting Dayem-bridges and a proposed classical thermodynamic model that seems to account for several of our experimental findings. In particular, zero-bias resistance and critical-current I_C measurements highlight the following: the suppression of I_C with both polarities of gate voltage, the surface nature of the effect, the independence of critical temperature from the electric field, and the gate-induced growth of a subgap dissipative component. In addition, the temperature dependence of the Josephson critical current seems to show a transition from ballistic Kulik-Omelyanchuk behavior to Ambegaokar-Baratoff tunnellike behavior on increase of the electric field. Furthermore, the I_C suppression persists in the presence of sizable perpendicular-to-plane magnetic fields. We propose a classical thermodynamic model able to describe some of the experimental observations of the present and previous work. Above all, the model grabs the bipolar-electric-field-induced suppression of I_C and the emergence of a subgap dissipative component near full suppression of the supercurrent. Finally, applications using the effect discussed are proposed.

DOI: 10.1103/PhysRevApplied.11.024061

I. INTRODUCTION

Metals are believed to be insensitive to the field-effect because an external electric field vanishes within a depth comparable to the Thomas-Fermi length (smaller than atom dimensions). However, there is no physical reason to exclude the possibility to modulate the conductivity of metallic thin films via charge accumulation or depletion. Starting from the 1950s, several gating experiments showed the impact of electrostatic charging on the conductivity of metallic thin films [1–3] and on the transition temperature of metallic superconductors [4,5]. Furthermore, recent calculations regarding gating on a metallic superconductor (Pb) showed that the perturbation to superconductivity due to an external electric field extends into the bulk of the superconductor for at least one coherence length [6]. Conventional solid gating allows one to realize electric fields on the order of a maximum of 10^9 V/m. As a consequence, the maximum variation of free-carrier concentration is about a few percent within the penetration depth of the electric field, which is reflected in a modulation of conductivity of the same order of magnitude [3]. Analogously, superconducting metallic thin films showed a change of the critical temperature T_C of a few percent when exposed to strong electric fields [4]. In particular, charge depletion caused an increase of normal-state resistance and a decrease of the critical temperature, while carrier accumulation caused lower resistance and higher critical temperature. The advent of electrolyte gating [7], which relies on the voltage-induced polarization of an electrolyte (which is an ionic conductor and an electronic insulator) between a counter electrode and the device, allowed the achievement of electric fields as large as 10^{10} V/m and surface carrier modulations of 10^{15} charges/cm^2 for gate voltages on the order of a few volts [8]. Therefore, conductivity modulations of about 10% have been demonstrated in metals [9,10], such as gold, copper, and silver, and sizable changes of the critical temperature of approximately 1% in metallic superconductors, such as for niobium [11] and niobium nitride [12], have been achieved. Recent

*federico.paolucci@nano.cnr.it

experiments investigated the dependence of both the critical current I_C and the critical temperature of metallic superconductors (aluminum and titanium) on conventional solid gating [13–15]. These studies focused on electric fields reaching maximum intensities on the order of 10^8 V/m, where the variation of charge-carrier concentration in metals is negligibly small. On the one hand, the normal-state resistance and the superconducting transition temperature were independent of the applied gate voltage; on the other hand, the critical current was suppressed for both polarities of the electric field [13,14]. These experimental results seem to exclude both charge accumulation/depletion and quasiparticle overheating at the origin of the supercurrent suppression, but a microscopic explanation of the phenomenon is still missing.

Here we describe an extensive set of solid-gating experiments performed on titanium-based Dayem-bridge field-effect transistors (DB FETs) and a superconducting thermodynamic model that seems able to support the phenomenology typical of several experimental observations presented in this work and in previous studies [13,14]. The article is organized as follows: Sec. II presents a basic characterization of the electric-field-dependent suppression of I_C and the study of the joint impact of two different electric fields on the critical current; Sec. III describes the evolution of the Josephson effect with gate voltage and its interpretation through a theory accounting for the change of the transmission probability of the junction; Sec. IV describes the temperature dependence of the resistance measured for different values of injection current and gate voltage; Sec. V describes the joint impact of electric and magnetic fields on both the critical temperature and the critical current of the Dayem-bridge; Sec. VI presents a classical thermodynamic model that seems able to explain some of the observations, such as the gate-voltage-induced suppression of the critical current and the invariance of the superconducting transition temperature; and Sec. VII describes in detail two possible applications of our devices in the framework of both quantum and classical computation.

II. BASIC CHARACTERIZATION OF THE FIELD-EFFECT

Figure 1(a) shows a schematic representation of a DB FET, where the top surface is a scanning electron micrograph of a real device and the electrical connections are represented. A typical gate-tunable Dayem-bridge Josephson junction (JJ) consists of a titanium (Ti) strip (approximately 4 μm wide and approximately 30 nm thick) interrupted by a constriction (approximately 125 nm long and approximately 300 nm wide). Two side electrodes [green and violet stripes in Fig. 1(a)] placed approximately $80-120$ nm from the constriction allow us to independently apply two different gate voltages V_{G1} and

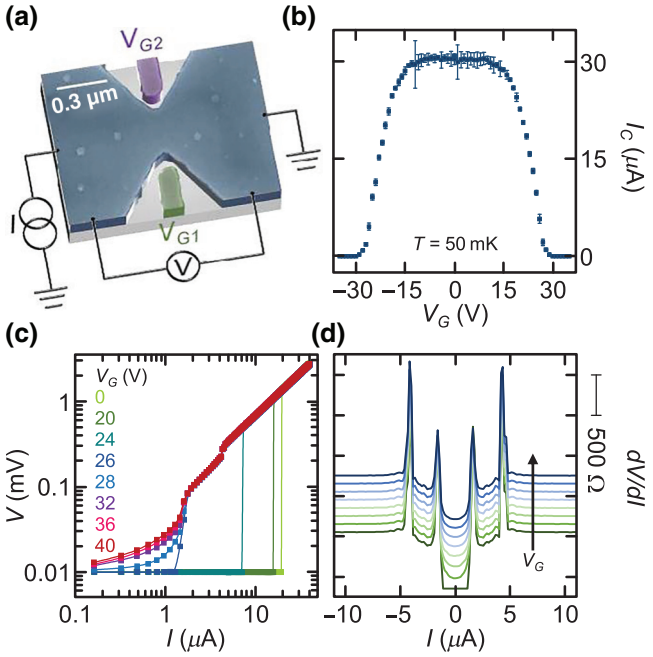

FIG. 1. (a) A typical FET device. The Josephson junction (blue) is current biased and the voltage drop is measured with a room-temperature voltage preamplifer, while the gate voltages V_{G1} and V_{G2} are applied to the bottom (green) and top (violet) lateral gate electrode, respectively. (b) Dependence of the critical current I_C on the gate voltage applied to both electrodes $V_G = V_{G1} = V_{G2}$ at a bath temperature $T = 50$ mK. (c) The log-log I-V characteristics of a DB FET measured at $T = 50$ mK for different gate voltages $V_G = V_{G1} = V_{G2}$. (d) Dependence of dV/dI on injection current I for $V_G = V_{G1} = V_{G2} = 26-40$ V with a step size of 2 V. The experimental traces are vertically shifted for clarity.

V_{G2} and, therefore, electric fields on the JJ region. The DB FETs are nanofabricated through single-step electron-beam lithography followed by evaporation of Ti on top of a p^{++}-doped silicon substrate covered with silicon dioxide (300 nm thick). The titanium thin films are deposited in the ultrahigh-vacuum chamber (base pressure on the order of 10^{-11} Torr) of an electron-beam evaporator at a rate of approximately 13 Å/s. The magnetoelectric characterization of the DB FETs is performed in a filtered ^{3}He-^{4}He dry dilution refrigerator (two-stage RC and π filters) by the standard four-wire technique. A direct current is injected with use of a low-noise source, the voltage across the bridge is measured by room-temperature preamplifiers, and a gate voltage is applied with use of a source-measure unit through different room-temperature low-frequency filters ($\tau \simeq 1-100$ s), with identical results.

Measurements of the superconducting critical current I_C as a function of the same voltage applied simultaneously to both gate electrodes (i.e., $V_G = V_{G1} = V_{G2}$) at a bath temperature $T = 50$ mK are shown in Fig. 1(b). In full agreement with the first demonstrations of

electric-field-dependent modulation of the critical current in metallic BCS superconductors [13,14], I_C is almost unaffected for low values of V_G and starts to monotonically reduce until its full suppression at a critical voltage $V_{GC} \simeq 26$ V (I_C is suppressed for both positive and negative values of the gate voltage). Notably, the field-effect-induced reduction of the critical current in our DB FETs is *symmetric* in the polarity of V_G. Since the intrinsic value of the chemical potential of the different stable phases of titanium does not reside at the van Hove singularity in the electron density of states [16,17] and the maximum superconducting correlation occurs at the van Hove singularity point, we can conclude that charge filling/depletion [11,12,18–20] cannot be the origin of such behavior [the critical current would increase (decrease) for charge filling (depletion)].

Figure 1(c) displays the I-V characteristics of a Dayem-bridge field-effect transistor measured for different gate voltages ($V_G = V_{G1} = V_{G2}$) at temperature $T = 50$ mK plotted on a double-logarithmic scale. On the one hand, for $V_G \leq 26$ V, the current flow is dissipationless ($V = 0$) under the critical current, while above I_C the I-V characteristics are completely Ohmic. On the other hand, for $V_G \geq 28$ V, charge transport is always dissipative ($V > 0$), but the Ohmic behavior ($V \propto I$) starts at $I \simeq 5$ μA independently of the gate voltage; furthermore, the emergence of a small jump in the I-V characteristics at about 4 μA is probably related to the transition into the normal state of a small portion of the device less affected by the electric field. The plots in Fig. 1(c) resemble the behavior of the critical current in an overdamped Josephson junction near the critical temperature in the presence of sizable thermal noise [21]. Since our measurements are performed at about $0.1T_C$ ($T_C \simeq 540$ mK) and there is no evidence of gate-dependent thermal (or even electrical) noise, we exclude such a mechanism as the origin of the effect presented.

The dissipative behavior in the transistors is emphasized by plotting the differential resistance dV/dI as a function of injection current I for different gate voltages around the critical value $V_{GC} = 28$ V [see Fig. 1(d)]. In particular, dV/dI shows a plateau under I_C only for $V_G = 26$ V, while for higher gate voltages the dissipative contribution at low injection current rises. Since the data are the numerical derivative of measurements acquired by sweeping the injection current from negative to positive values, the peaks for $I < 0$ represent the retrapping current I_R, whereas the spikes for $I > 0$ indicate the critical current I_C. Notably, I_R stays almost constant in the range of applied gate voltages. The traces in Fig. 1(d) show two main features. First, the Dayem-bridge exhibits two transitions for gate voltages approaching V_{GC} [see also Fig. 1(c)]. Second, only for $V_G > 26$ V are the critical current and the retrapping current of both transitions equal ($I_R = I_C$, because the critical current lowers and the retrapping current cannot exceed I_C), as reported in previous gating experiments on BCS wires [13].

To study the impact of the electric field on a superconducting metal and its effect on I_C, we measure the critical current while applying two independent voltages, V_{G1} and V_{G2}, to the side gate electrodes. The contour plots in Figs. 2(a) and 2(b) show the normalized critical current I_C/I_{C0} (where I_{C0} is the critical current with no gate voltage applied) as a function of both V_{G1} and V_{G2} measured for two different DB FETs at $T = 50$ mK. The gate electrodes in device 1 are placed about 120 nm from the constriction, while in device 2 they are separated by a gap of approximately 80 nm. The color plots of our DB FETs show a squarelike shape [the rectangular shape in Fig. 2(a) stems from the different distance of the two gates from the active region] that indicates the *independence* of the effects of V_{G1} and V_{G2} on the critical current. This behavior is highlighted by the plots of I_C/I_{C0} as a function of V_{G1} (V_{G2}) for fixed values of V_{G2} (V_{G1}) shown in Fig. 2(c) and 2(d) for the contour plot of Fig. 2(b). On the one hand, the traces confirm the independence of the critical voltage of one gate from the other. On the other hand, the plots highlight a similar reduction effect of V_{G1} and V_{G2} on I_C. The small asymmetry existing with the sign of V_{G1} and V_{G2} arises from the experimental procedure followed to perform the experiments: both gate voltages are swept from negative to positive values. As a consequence, because of

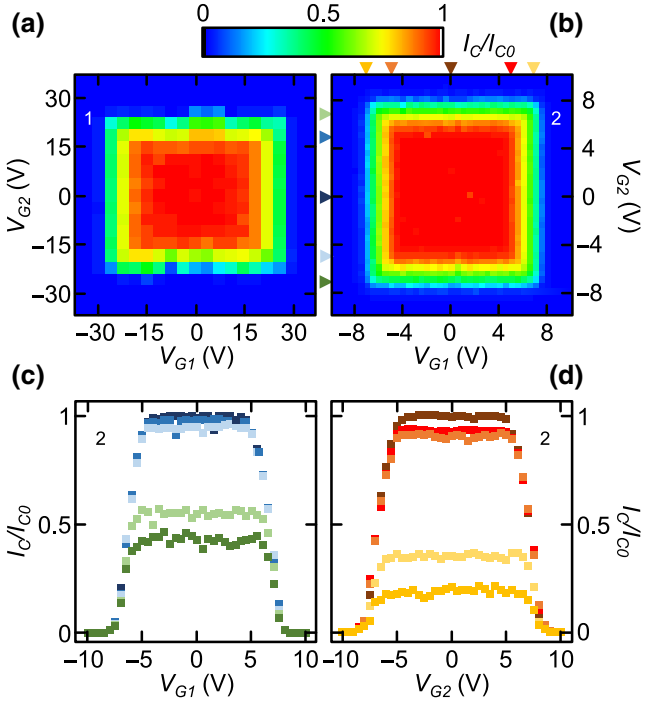

FIG. 2. (a),(b) Color plot of the normalized critical current I_C/I_{C0} as a function of V_{G1} and V_{G2} measured at a bath temperature $T = 50$ mK for two different devices (1 and 2). (c) I_C/I_{C0} versus V_{G1} for different values of V_{G2} indicated by the arrows in (b). (d) I_C/I_{C0} versus V_{G2} for different values of V_{G1} indicated by the arrows in (b).

a small hysteresis in the electric field response, the critical current is slightly smaller for negative gate voltages $[I_C(-V_G) \lesssim I_C(V_G)]$.

The phenomenology related to the dependence of the effect of V_{G1} and V_{G2} on I_C seems to suggest that the suppression of the critical current is related to a surface effect, which nonlocally affects the superconductivity within a distance of a few times the superconducting coherence length ξ. Specifically, in experimental conditions similar to those of the present measurements (i.e., in solid-gated Ti wires far below T_C), the electric-field-induced suppression of the critical current has been shown to extend into the superconductor bulk for a few times the coherence length [13].

III. JOSEPHSON EFFECT

The Dayem-bridge geometry chosen for our devices allows us to study the dependence of the Josephson coupling on the applied gate voltage $V_G = V_{G1} = V_{G2}$. The left panels in Figs. 3(a) and 3(b) show the dependence of the critical current I_C on the bath temperature T measured for different values of V_G. By increasing the gate voltage, on the one hand, the critical current is suppressed at every temperature in the measured range ($T <$ 600 mK), while, on the other hand, the Josephson supercurrent vanishes always at the same bath temperature T; that is, the temperature when no gate bias is applied ($T_C \simeq 540$ mK). The suppression of I_C in a Josephson junction due to injection of quasiparticles generated by V_G would increase the effective electronic temperature T_{eff} [22]. Therefore, the Josephson supercurrent would vanish ($I_C = 0$) when $T_{\text{eff}} = T_C$, but $T < T_C$. As a consequence, we can reasonably exclude quasiparticle overheating as the source of critical-current suppression in our DB FETs.

Further analysis of the data shows that I_C of the pristine JJ (i.e., with $V_G = 0$) has the typical Kulik-Omelyanchuk dependence [24] on temperature characteristic of a clean ballistic constriction, while near-full Josephson-supercurrent suppression ($V_G \simeq V_{GC}$) the device has Ambegaokar-Baratoff behavior [25] as a tunnel JJ [see the left panels in Figs. 3(a) and 3(b)].

The critical current of a Josephson constriction in the short-junction limit can be written as [23]

$$I_C(\varphi) = \frac{\pi\Delta}{2eR_N}\frac{\sin\varphi}{\sqrt{1-\mathcal{T}\sin^2\frac{\varphi}{2}}} \times \tanh\left(\frac{\Delta}{2T}\sqrt{1-\mathcal{T}\sin^2\frac{\varphi}{2}}\right), \quad (1)$$

where φ is the phase difference across the JJ, Δ is the pairing potential, e is the electron charge, $\mathcal{T}$ is the

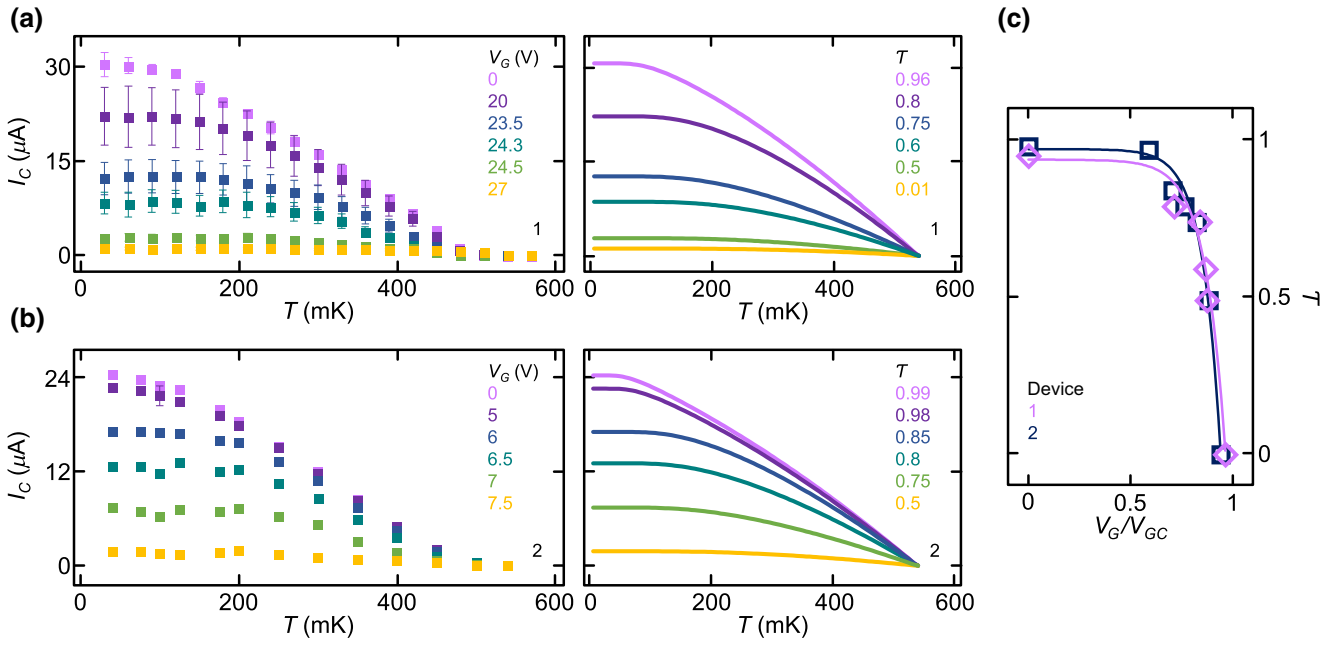

FIG. 3. (a),(b) Critical current I_C as a function of the bath temperature T for different gate voltages $V_G = V_{G1} = V_{G2}$ measured on devices 1 and 2, respectively (left), and fit of the behavior of I_C versus T calculated with the Kulik-Omelyanchuk theory generalized for an arbitrary effective transmissivity $\mathcal{T}$ of the Josephson junction [23] (right). The extracted values of $\mathcal{T}$ correspond to the gate voltages represented by the same color in the left panel. (c) Effective transmissivity $\mathcal{T}$ of the JJ versus normalized gate voltage V_G/V_{GC} extracted for device 1 (purple) and device 2 (blue).

transmission probability and R_N is the contact normal-state resistance. The latter can be written as $R_N = R_{\rm Sh}/\mathcal{T} = (4\pi^2\hbar)/(e^2 k_F^2 S\mathcal{T})$, where $R_{\rm Sh}$ is the Sharvin resistance, k_F is the Fermi wave vector, and S is the constriction cross-section area. For $\mathcal{T} = 1$, Eq. (1) adheres to the Kulik-Omelyanchuk advanced theory [24], whereas for $\mathcal{T} \ll 1$, it reduces to the Ambegaokar-Baratoff model [25].

We fit the experimental data using Eq. (1). The right panels in Figs. 3(a) and 3(b) show the theoretical traces calculated for the experimental curves in the left panels (the values of $\mathcal{T}$ correspond to values of V_G represented with the same color). We stress that in our experiments the normal-state resistance is unaffected by the electric field. To use this model nevertheless, we take a phenomenological point of view and assume that some channels do not contribute to the supercurrent. The microscopic mechanism for how this would occur is, however, unclear at present. However, the fits show good agreement with the experimental data. In particular, the experimental curves measured for increasing gate voltage correspond to theoretical curves calculated for decreasing effective transmission probability. The theory is not able to grasp the change of concavity in the I_C-versus-T trace near the critical temperature when a gate voltage is applied. This model considers a temperature-independent transmission probability. However, since the effectiveness of the critical-current suppression in similar structures has been shown to decrease on increase of the temperature [13,14], we can speculate that the value of $\mathcal{T}$ arising from the analysis of the present data should be temperature dependent (especially near T_C).

To compare FET devices with gate electrodes placed at different distances from the JJ, we plot $\mathcal{T}$ as a function of the normalized gate voltage V_G/V_{GC} [see Fig. 3(c)]. Despite the critical voltages of the two transistors being extremely different ($V_{GC}^1 \simeq 4V_{GC}^2$, where V_{GC}^1 and V_{GC}^2 are the critical voltages of device 1 and device 2, respectively), the effective transmission probability seems to show a universal dependence on the normalized gate voltage. In particular, $\mathcal{T}$ drastically reduces near V_{GC}, suggesting the gate-induced creation of dissipative regions in the Dayem-bridge not able to carry the Josephson supercurrent. Furthermore, the dissipative states observed in the I-V characteristics at high values of V_G [as shown in Fig. 1(c)] seem to indicate the formation of disordered puddlelike normal-metal–superconducting regions with a noncontinuous superconducting path.

In summary, the entire phenomenology of the Josephson critical current seems to be compatible with the growth of dissipative regions in the Dayem-bridge constriction by increase of the gate voltage and the creation of a percolative path for the Josephson current translated in the reduction of the effective transmission probability of the junction.

IV. TEMPERATURE DEPENDENCE OF RESISTANCE

The resistance-versus-temperature characteristics of the FETs are obtained by a low-frequency lock-in technique for different gate voltages applied by a low-noise source-measure unit. The voltage drop is amplified through room-temperature differential amplifiers. To evaluate the interplay of the bias current with the gate voltage on the superconductor-to-normal-metal transition, we repeat the experiments for two values of the current, $I = 400$ pA and $I = 1$ nA. In both cases we measure a resistance in the normal state $R_N \simeq 600\ \Omega$, in agreement with the I-V characteristics in Fig. 1(c). Figures 4(a) and 4(c) show the temperature dependence of the normalized resistance R/R_N for selected values of the gate voltage measured with $I = 400$ pA and $I = 1$ nA, respectively. In agreement with previous reports on gating of metallic wires [13] and Dayem-bridges [14], the critical temperature stays constant within experimental error for all values of V_G studied. On the other hand, a subgap dissipative component starts to grow at high gate voltages for both injected currents [see Figs. 4(a) and 4(c)].

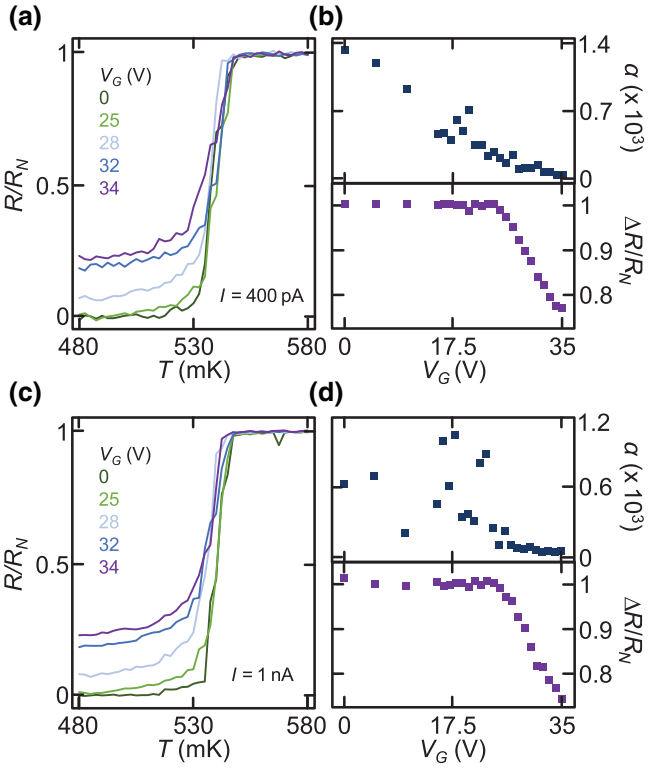

FIG. 4. (a),(c) Normalized zero-bias resistance R/R_N as a function of temperature T measured in device 1 for different gate voltages $V_G = V_{G1} = V_{G2}$ with 400-pA current bias (a) and 1-nA current bias (c) current. (b),(d) Electrothermal parameter α (top panel) and normalized resistance jump at the superconductor–normal-metal transition $\Delta R/R_N$ (bottom panel) as a function of gate voltage $V_G = V_{G1} = V_{G2}$ for 400-pA current bias (b) and 1-nA current bias (d).

To highlight the dependence of the resistance on both temperature and electric field and to give a quantitative analysis of the data, we introduce two dimensionless figures of merit: the *electrothermal* parameter α [26] and the normalized resistance jump between the superconducting state and the normal state.

The parameter $\alpha = [T/R(T,I)]/[dR(T,I)/dT]$, where the resistance R depends on both temperature T and bias current I, characterizes the sharpness of the superconducting transition. The top panels in Figs. 4(b) and 4(d) show the dependence of the electrothermal parameter α calculated at half of the superconductor–normal-metal transition (i.e., when $R = R_N/2 \simeq 300\ \Omega$) as a function of gate voltage for $I = 400$ pA and $I = 1$ nA, respectively. For all values of V_G, the transition is sharper (i.e., α assumes higher values) for low applied bias, because the depairing probability increases with biasing current [27]. On increase of the gate voltage, α decreases because the superconducting transition widens in temperature and decreases in height [see Figs. 4(a) and 4(c)]. The electrothermal parameter shows strong fluctuations with V_G in correspondence with the beginning of the critical-current suppression [see Fig. 1(b)]. At these gate voltages, the critical-current noise rises [13,14] because the electric field apparently causes more instabilities to the superconducting condensate. The latter is reflected in a randomization of the superconducting transition and a fluctuating α especially for higher bias current (where the depairing is naturally stronger).

The normalized resistance jump across the superconducting transition is defined as $\Delta R/R_N = [R(T = 480\,\text{mK}) - R_N]/R_N$ and is a way to quantify the growth of the zero-bias dissipative component with gate voltage [see the bottom panels in Figs. 4(b) and 4(d)]. The latter starts to decrease at $V_G \simeq 25$ V for both injection currents. On further increase of the gate voltage, the normalized resistance jump decreases almost linearly to approximately 0.75 for $V_G = 35$ V [where $I_C = 0$; see Fig. 1(b)] with a small difference (a few percent) between the two bias currents. The growth of the zero-bias dissipative component below the critical temperature (in the following denoted by R_{sup}) once more seems to suggest the creation and manifestation of normal-metal regions interrupting the superconductor and establishing a percolative pattern for the Josephson supercurrent. Furthermore, the invariance of R_{sup} with the current seems to indicate that the remaining superconducting regions can support a higher supercurrent, as evident from the low-temperature I-V characteristics shown in Fig. 1(c).

V. JOINT IMPACT OF ELECTRIC AND MAGNETIC FIELDS

The interplay between the electric field and the magnetic field is investigated both by zero-bias experiments (R vs B at fixed V_G) and by critical-current measurements (I_C vs V_G at fixed B). The experimental setups were presented in Secs. II and IV, and the magnetic field is applied out of the plane (perpendicular to the superconducting film).

We first present the evolution of the critical magnetic field B_C with gate voltage V_G measured with an injection current $I = 1$ nA at a bath temperature $T = 50$ mK [see Fig. 5(a)]. On the one hand, the onset of the superconducting transition seems to slightly change with increasing gate voltage. On the other hand, the width of the transition increases with gate voltage until a resistive component grows even at $B = 0$ [in agreement with the R-vs-T experiments shown in Figs. 4(a) and 4(c)].

To quantify the evolution of the critical magnetic field with the gate voltage, we extrapolate the values of B_C at the onset and a half and full transition, as shown in Fig. 5(b). We define the onset of the transition as the values of the magnetic field corresponding to a zero-bias resistance of 600 Ω [$B(R = 600\ \Omega)$]. The onset of the transition stays almost constant until the gate voltage reaches the critical value $V_{GC} = 18$ V, and then the critical field slowly and almost linearly decreases to about the 10% of its intrinsic value. The half-transition magnetic critical field (i.e., the value of B for which $R = R_N/2 \simeq 300\ \Omega$) monotonically decreases from $B \simeq 115$ mT at $V_G \leq 18$ V to $B \simeq 74$ mT at $V_G = 35$ V (with a total variation of about 35%). Finally, the zero-resistance critical field drops very steeply with gate voltage (in the range 18–29 V) from $B \simeq 100$ mT to $B = 0$. The total suppression of the zero-resistance critical field highlights the growth of a subgap dissipative component as already reported in zero-bias experiments performed at temperatures close to T_C [see Figs. 4(a) and 4(c)].

The resistance in the superconducting state R_{sup} increases with temperature for a fixed value of gate voltage, as shown in Fig. 5(c). This effect can be interpreted in terms of strengthening of the depairing of the Cooper pairs and the increasing probability of transition to the normal state of small superconducting areas with rising temperature.

In summary, the measurements of zero-bias resistance as a function of magnetic field for different gate voltages provide useful information on the origin of the suppression of the Josephson critical current. On the one hand, the (almost) invariance of the transition onset for large V_G values suggests the exclusion of quasiparticle overheating as the origin of the suppression of superconductivity, because the transition onset is expected to decrease more evidently on increase of the electronic temperature [28]. On the other hand, the behavior of the three critical fields highlights the broadening of the normal-metal-to-superconductor transition, which increases from approximately 27 mT to approximately 100 mT, which could be due to the formation of normal-metal areas. Possibly these normal portions could affect the dependence of the zero-bias resistance on the magnetic field due to an inverse proximity effect

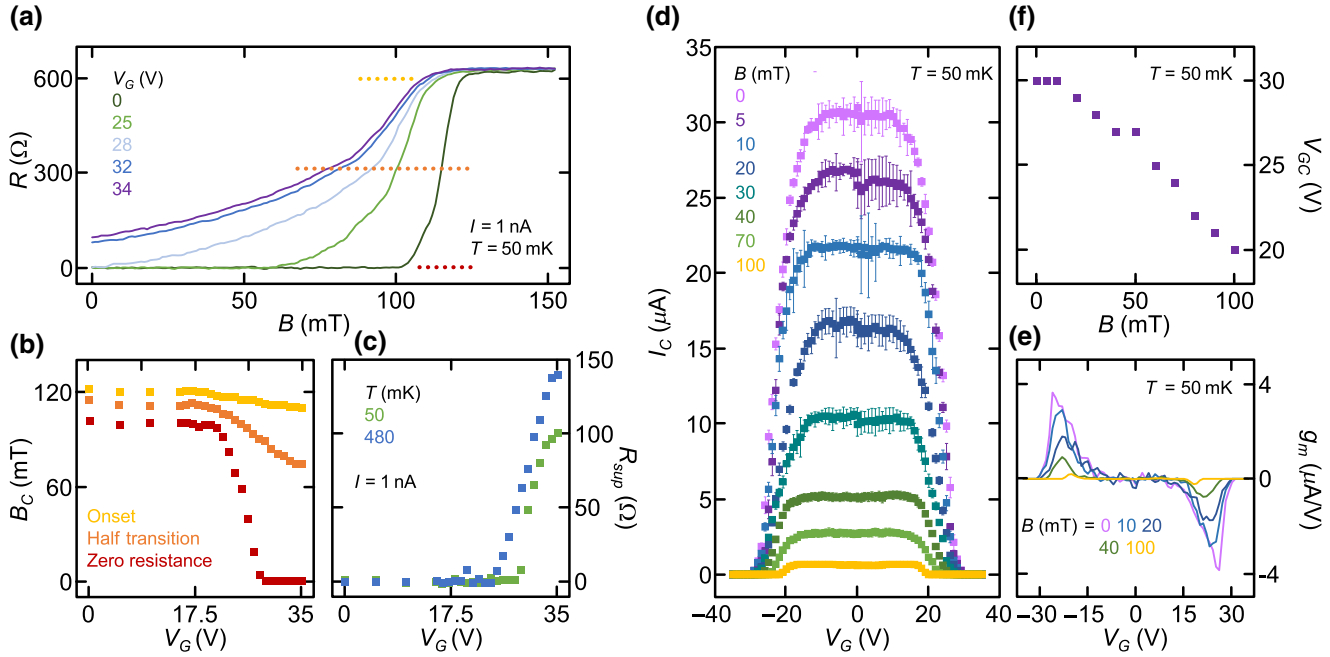

FIG. 5. (a) Zero-bias resistance R as a function of the perpendicular magnetic field B measured at $T = 50$ mK for gate voltages $V_G = V_{G1} = V_{G2}$ with 1-nA current bias. (b) Critical magnetic field B_C extracted from R-versus-B measurements (a) at the onset of transition (yellow), half transition (orange), and complete transition (red) to the superconducting state. (c) Resistance in the superconducting state $R_{\rm sup}$ as a function of gate voltage $V_G = V_{G1} = V_{G2}$ measured at $T = 50$ mK [green, extracted from data in (a)] and $T = 480$ mK [blue, extracted from data in Fig. 4(c)] with 1-nA current bias. (d) I_C versus $V_G = V_{G1} = V_{G2}$ measured at $T = 50$ mK for different values of the perpendicular-to-plane magnetic field B. (e) Transconductance g_m as a function of gate voltage $V_G = V_{G1} = V_{G2}$ measured at $T = 50$ mK for different values of B. (f) Critical gate voltage V_{GC} as a function of the perpendicular magnetic field B measured at $T = 50$ mK.

[29,30], but the lack of a microscopic description of the effect impedes quantification of their real impact.

We now focus on the combined impact of electric and magnetic fields on the critical current in the Dayem-bridge field-effect transistors. Figure 5(d) shows the dependence of I_C on V_G for different values of the perpendicular-to-plane magnetic field. The critical-current suppression is almost invariant with the polarity of the electric field, the plateau of constant I_C widens with increasing magnetic field, and the critical voltage for full suppression of the Josephson supercurrent V_{GC} decreases with rising B. These results resemble those reported in similar experiments performed on superconducting wires [13] that do not have a microscopic explanation yet (a phenomenological ad hoc Ginzburg-Landau model was used to make a comparison with the data [13]). The widening of the plateau with rising magnetic field suggests again the exclusion of quasiparticle overheating as the origin of supercurrent suppression because the dependence of I_C on B is steeper for temperatures approaching T_C [31].

To highlight the decrease of the critical-current modulation with the gate voltage for increasing magnetic field, we calculate the transconductance $g_m = dI_C/dV_G$ as a function of V_G for different values of B, as plotted in Fig. 5(e). The transconductance decreases by more than 1 order of magnitude with increasing magnetic field and its maximum value moves toward lower electric fields (in both positive and negative polarity) with increasing B. In particular, the maximum transconductance varies from approximately 3.6 μA/V at $V_G = 26$ V for $B = 0$ to approximately 0.2 μA/V at $V_G = 18$ V for $B = 100$ mT.

The critical voltage is almost constant for small values of the magnetic field and then decreases almost linearly with B [see Fig. 5(f)] from $V_{GC} \simeq 30$ V at $B = 0$ to $V_{GC} \simeq 20$ V at $B = 100$ mT. The variation of V_{GC} with the magnetic field is much stronger than with the temperature [14] and resembles the behavior reported for solid-gated superconducting metal wires [13]. All this phenomenology has no microscopic explanation yet.

VI. THERMODYNAMIC MODEL

The above experimental evidence and recent findings with regard to electric-field-dependent supercurrent suppression in metallic superconductors [13,14] still lack a complete microscopic interpretation. Here, by starting with a simple working hypothesis, we develop a classical thermodynamic model [29,30] accounting for several experimental observations.

We consider a rectangular superconducting wire with dimensions L_x, L_y, and L_z at temperature $T < T_C$ subjected to a lateral electric field $\vec{E}$ pointing to the center of the sample, as shown in Fig. 6. Our theory is grounded on one key hypothesis: the electrostatic energy stored in a superconductor is assumed to be larger than that stored in a normal metal. This excess electric energy in the superconductor could be due to an increase of the electric penetration length λ_S and/or an increase of the permittivity ϵ_S, as theoretical studies on bulk superconductors [32–34] and experimental observations on thin films [35] seem to indicate. As a consequence, our working hypothesis can be reduced to the assumption that $\theta = \lambda_S\epsilon_S - \lambda_N\epsilon_N > 0$, where λ_N and ϵ_N are the penetration length and the permittivity in the normal state, respectively. Notably, under this condition, superconductivity becomes *unstable* when the excess electrostatic energy stored in the superconductor is comparable to its condensation energy. To simplify the discussion, we assume that the electric field is constant within the region penetrated by the electric field. The latter is a realistic hypothesis given that the distance of the gate electrodes from the superconductor (approximately 80–120 nm) is much larger than the electric-field-penetrated region (less than 1 nm [6,12]).

We denote with F_S and $\mathcal{F}_S$ the free-energy density and the free energy associated with the superconductor, respectively. We use analogous notation F_N and $\mathcal{F}_N$ for the normal region. By following the standard thermodynamic approach [29,30,36] we can write the free energies associated with the superconducting state and the normal state as

$$\begin{aligned} \mathcal{F}_S &= V_S F_S + V_{S,E}^T u_{E,S}, \\ \mathcal{F}_N &= V_N F_N + V_{N,E}^T u_{E,N}, \end{aligned} \tag{2}$$

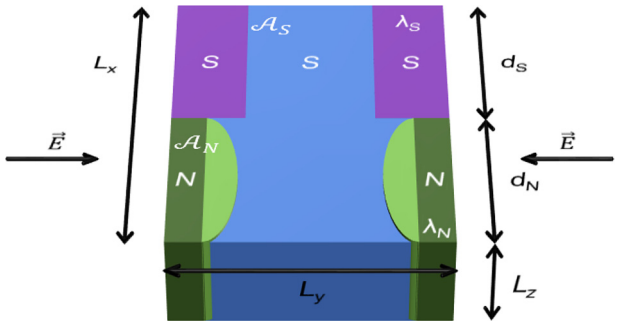

FIG. 6. Superconducting wire of dimensions L_x, L_y, and L_z subjected to a lateral electric field $\vec{E}$ along the y direction. λ_S and λ_N are the lengths of electric field penetration into the superconducting region (S; blue and violet) and the normal region (N; dark and light green), respectively. $\mathcal{A}_S$ and $\mathcal{A}_N$ are the areas of the superconducting and normal regions, respectively. The boundary regions exposed to the electric field have lengths d_S and d_N, respectively.

where V_S is the superconductor volume, V_N is the normal-metal volume, $V_{S,E}^T$ and $V_{N,E}^T$ are the volumes of the superconductor and the normal metal penetrated by the electric field, respectively, and $u_{E,S} = \frac{1}{2}\epsilon_S E^2$ and $u_{E,N} = \frac{1}{2}\epsilon_N E^2$ are the electric field energy densities. It is important to point out that from previous experiments [12–14] and theoretical calculations [6] it turns out that, to observe the electric field-effect, the length along which we apply the electric field is at most a few times the coherence length. The present classical model does not account for this microscopic information. In the following we assume to be in this case.

A. Superconductor-to-normal-metal transition

Here we focus on the case when all the wire is in the superconducting state or in the normal state, and thus, with respect to Fig. 6, we assume that $d_N = 0$ or $d_S = 0$ (i.e., $V_S = V$ or $V_N = V$, where $V = L_x L_y L_z$ is the total volume). Accordingly, the volumes of the superconductor or the normal metal penetrated by the electric field $\vec{E}$ can be written as $V_{S,E}^T = L_z L_x (2\lambda_S)$ or $V_{N,E}^T = L_z L_x (2\lambda_N)$, where the factor 2 stems from the electric field applied to both sides of the specimen.

In the presence of a static electric field, the superconducting state is energetically favorable when $\mathcal{F}_N > \mathcal{F}_S$. With the generic volume expressions, this inequality reads

$$\mathcal{U}_{E,S} - \mathcal{U}_{E,N} = \Delta\mathcal{U}_E < V\Delta F, \tag{3}$$

where $\mathcal{U}_{E,S}$ and $\mathcal{U}_{E,N}$ are the electric field energies in the superconductor and the normal metal, respectively, and $\Delta F = F_N - F_S$ is the condensation-energy density. This equation determines the electrical critical energy for which superconductivity is destroyed.

At $T = 0$, the condensation-energy density can be written as $\Delta F = N_0\Delta_0^2/2$ [30], where Δ_0 is the zero-temperature zero-field superconducting energy gap and N_0 is the density of states in the metal at the Fermi level. From Eq. (3), we can define the critical electric field for the superconductor-to-normal-metal transition as

$$E^2 < E_C^2 = \frac{L_y}{2\theta} N_0 \Delta_0^2. \tag{4}$$

To give a rough estimate of E_C and compare it with the experimental values, we use the parameters extracted from our measurements. The width of the device can be extracted from the typical dimension of the constriction, $L_y = 300$ nm. The titanium energy gap is given by $\Delta_0 = 1.764 k_B T_C = 82\ \mu$eV, where $T_C \simeq 540$ mK, and its density of states $N_0 = 1.35 \times 10^{47}\ \mathrm{J^{-1}\,m^{-3}}$ [13]. Since the permittivities for both the superconductor and the normal metal are unknown and their difference is small [32–34], we assume both of them to be equal to the vacuum permittivity (i.e., $\epsilon_S = \epsilon_N = \epsilon_0 = 8.85 \times 10^{-12}\ \mathrm{F/m}$). An

electric field penetrates a normal metal to a depth comparable to the Thomas-Fermi screening $\lambda_{T\text{-}F}$; therefore, we have $\lambda_N = \lambda_{T\text{-}F} = 0.5 \times 10^{-10}$ m. For a superconductor we assume a penetration depth $\lambda_S = \delta\lambda_N$, with the unknown scaling parameter $\delta > 1$ since we assume longer penetration in the superconductor than in the normal metal. In previous work on linear response of bulk superconductors, the values of δ approached 1 [32,33]. Notice that the critical electric field changes weakly with λ_S because of the square-root dependence in Eq. (4).

We now compare the theoretical values of E_C with the values extrapolated from the experimental data. With $\delta = 1.1$, we get $E_C = 2.8 \times 10^8$ V/m, while with $\delta = 1.01$, the critical electric field is 8.9×10^8 V/m. In device 1, the critical gate voltage $V_{GC} \simeq 30$ V with gate electrodes at a distance $d \simeq 120$ nm from the constriction yields a critical electric field $E_C = V_{GC}/d \simeq 2.5 \times 10^8$ V/m. In device 2, $V_{GC} \simeq 10$ V ($d \simeq 80$ nm) and, as a consequence, $E_C \simeq 1.25 \times 10^8$ V/m. We can conclude that the theoretical model is compatible with our experimental results given a small deviation of the screening length of about 1%–10%, which is sufficient for the observed superconductor-to-normal-metal transition.

B. Inhomogeneous state

The experimental data show the growth of a subgap dissipative state induced by the application of an external electric field [see Figs. 1(c), 4(a), 4(c), 5(a), and 5(c)] in agreement with previous results of gating experiments on metallic superconductors [14]. In the following we show how our thermodynamic model can also account for the appearance of an inhomogeneous state (where the superconductor and the normal state coexist in the wire) inducing a dissipative component in the transport characteristics.

In the superconductor–normal-metal inhomogeneous state the total volume of the wire can be divided into superconducting and normal-metal portions, $V = V_S + V_N$. Therefore, Eq. (2) has to take into account the superconductor and normal-state reduced volumes $V_S = L_z\mathcal{A}_S$ and $V_N = L_z\mathcal{A}_N$, where $\mathcal{A}_S$ and $\mathcal{A}_N$ are the superconducting and normal-metal surfaces, respectively (see Fig. 6), and they are related by $\mathcal{A} = L_xL_y = \mathcal{A}_S + \mathcal{A}_N$ (i.e., the total area needs to be conserved). In particular, we assume that the region directly exposed to the electric field is divided into superconducting and normal-metal areas, $L_x = d_S + d_N$, where d_S is the superconducting portion and d_N is the dissipative section. As a consequence, the free energies for the superconducting and normal states can be written as $\mathcal{F}_S = V_SF_S + V^T_{S,E}u_{E,S}$ and $\mathcal{F}_N = V_NF_N + V^T_{N,E}u_{E,N}$, and the total energy associated with this configuration is $\mathcal{F}_S + \mathcal{F}_N$.

We also need to consider the free-energy contribution at the superconductor–normal-metal interface since when we pass from a superconducting to a normal region, the order parameter ψ must change [29]. According to the Ginzburg-Landau theory, the latter gives a contribution to the free energy proportional to $\nabla\psi$. We denote the wall energy associated with the interface by $\mathcal{F}_W = L_zl\gamma$, where l is the total length of the interface and γ is the surface energy per unit area [29]. Therefore, the most-general expression for the *inhomogeneous*-state free energy reads

$$\mathcal{F}_I = V_SF_S + V^T_{S,E}u_{E,N} + V_NF_N + V^T_{N,E}u_{E,S} + \mathcal{F}_W. \quad (5)$$

To have an inhomogeneous state, in addition to the condition in Eq. (3), we require that $\mathcal{F}_S(V_S = V) > \mathcal{F}_I$ and $\mathcal{F}_N(V_N = V) > \mathcal{F}_I$, (i.e., the superconductor–normal-metal state is energetically favorable with respect to both the fully superconducting state and the normal state). If we consider the spatial distributions of the superconducting and normal regions, $V^T_{S,E} = L_zd_S(2\lambda_S)$ and $V^T_{N,E} = L_zd_N(2\lambda_N)$ (see Fig. 6), the above inequalities reduce to

$$\begin{aligned} &L_z\mathcal{A}_S\Delta F - L_zd_SE^2(\lambda_S\epsilon_S - \lambda_N\epsilon_N) - F_W > 0, \\ &-L_z\mathcal{A}_N\Delta F + L_zd_NE^2(\lambda_S\epsilon_S - \lambda_N\epsilon_N) - F_W > 0. \end{aligned} \quad (6)$$

We rewrite the superconducting and normal-metal areas as $\mathcal{A}_S = \chi\mathcal{A}$ and $\mathcal{A}_N = (1-\chi)\mathcal{A}$ and the exposed lengths as $d_S = \eta L_x$ and $d_N = (1-\eta)L_x$. It is also convenient to rescale the electric field over the critical electric field [see Eq. (4)] and define the ratio $\kappa = \frac{F_W}{V\Delta F}$. From a physical point of view, χ, η, and κ are related to the energy of the superconductor (through the area $\mathcal{A}_S$), the energy stored in the superconductor in the presence of an electric field (since d_S is the length of the superconductor exposed to the electric field), and the superconductor–normal-metal interface energy (through F_W). We can now write the above equations as

$$\frac{1-\chi+\kappa}{1-\eta} < \left(\frac{E}{E_C}\right)^2 < \frac{\chi-\kappa}{\eta}. \quad (7)$$

The necessary condition to have an electric field that can satisfy these inequalities is $\chi > \kappa + \eta$ and gives the spatial dimensions of the region over which the inhomogeneous state is energetically favorable.

A more-quantitative description of the distributions of the superconducting and metallic regions would need a microscopic theory, because the present theory is not able to predict the value of $F_W = L_zl\gamma$. In particular, it gives a boundary on the total area $\mathcal{A}_S$ but it is not able to predict the length l of the superconductor–normal-metal interface. In addition, the surface energy γ can be estimated only with the aid of a microscopic theory. The Ginzburg-Landau formalism (generally used in similar situations) gives information only when the order parameter can change over the coherence length ξ [29,30]. In the present

experiment, L_y and L_z are shorter than or of the same order as ξ, so the Ginzburg-Landau theory does not hold and it fails to predict the superconductor–normal-metal surface energy.

Despite these limitations, the simple classical thermodynamic model presented in this work predicts (for certain parameters and electric fields) the emergence of an inhomogeneous state induced by the static electric field. The latter is compatible with the experimental observations emerging both in the I-V characteristics and in the zero-bias resistance for high gate voltages (i.e., the electric field).

VII. POSSIBLE APPLICATIONS

The phenomenology presented in the above experimental sections of this work could pave the way to the design of a number of superconducting devices with gate-tunable behavior and performance, such as interferometers [37–39], photon detectors [40], parametric amplifiers [41], coherent caloritronic systems [42–46], metallic gate-tunable transmons ("gatemons") [47,48], and electric-field-controlled cryotrons [49,50]. In the following, we focus on the last two of the aforementioned applications.

The Josephson coupling energy E_D is related to the junction critical current I_C by $E_D = \hbar I_C/2e$, where $\hbar$ is the reduced Planck constant and e is the electron charge. Therefore, the tunability of the Josephson critical current of our Dayem-bridge field-effect transistors [see Fig. 1(b)] is reflected in the possibility of controlling E_D across at least 2 orders of magnitude, as shown in Fig. 7(a). This capability is nowadays exploited to implement superconducting qubits in the form of gate-tunable semiconductor-based transmons [47,48], so-called gatemons. Similarly, our DB FETs could be the key element for the realization of fully metallic gate-tunable Dayem-bridge transmons, the "dayemons". In such a configuration, the qubit is composed of the DB FET shunted by a capacitance C_S and is capacitively coupled to a transmission-line resonant cavity [47] as depicted in Fig. 7(b). If the Josephson energy is far greater than the charging energy ($E_D \gg E_C$), the qubit transition energy takes the form $f_Q \simeq \sqrt{8E_C E_D}/h$, where the charging energy can be calculated from the total capacitance $C_{\rm tot}$ through $E_C = e^2/2C_{\rm tot}$ [47]. By assuming $C_{\rm tot} = 100$ fF, we can calculate the expected qubit frequency for different gate voltages applied to our DB FETs. For both devices presented, the qubit frequency can be tuned by more than 1 order of magnitude by change of V_G. In particular, for device 2 the value of f_Q stays constant for gate voltages reaching 4 V [$f_Q(V_G = 0 - 4\text{V}) \simeq$ 135 GHz] and then monotonically decreases with further rise of V_G [$f_Q(V_G = 6.8\text{V}) \simeq 88$GHz and $f_Q(V_G = 7.5\text{V}) \simeq 28$GHz]. On the one hand, the dayemons are predicted to show performance similar to that of conventional semiconductor-based transmons (gatemons) [47,48]. On the other hand, dayemons have a *monolithic* architecture: they are made of a single superconducting metal without any interface between different materials and any oxidation process. Therefore, this is a robust and scalable technology for the implementation of superconducting qubits.

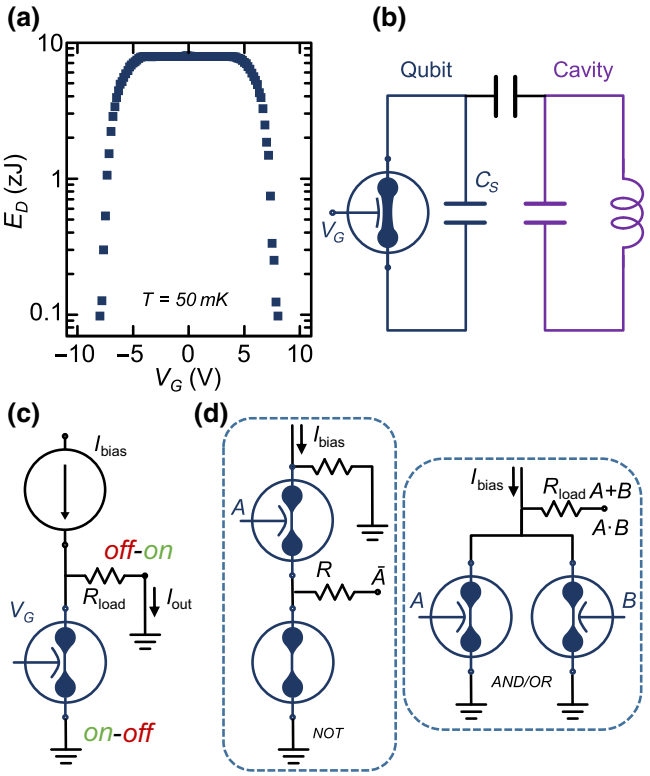

FIG. 7. (a) Josephson coupling energy E_D as a function of the gate voltage V_G for device 2 at $T = 50$ mK. (b) The dayemon device, where the qubit and the capacitively coupled resonant cavity are represented. (c) The electric-field-controlled cryotron. (c) Classic logic gates based on the electric-field-controlled cryotron: NOT, AND, and OR.

The modulation of the critical current through an external gate electrode is one of the key elements of superconducting classical computation [51]. Recently, the challenge has been addressed by the development of nanocryotrons, the so-called *nTrons*, which use an input gate current to tune the supercurrent transport of a metallic channel [49,50]. Analogously, the DB FET can be used to realize an electric-field-controlled cryotron, as depicted in Fig. 7c, with the advantage of a very large input-to-output impedance. The bias current is chosen to be lower than the film intrinsic critical current ($I_{\rm bias} < I_{C0}$); therefore, for $V_G = 0$ all the current flows into the transistor and the output current is zero ($I_{\rm out} = 0$). When $I_{\rm bias} > I_C(V_G)$, the channel switches to the normal state and $I_{\rm out} \neq 0$. In our device we can use $I_{\rm bias} = 10\ \mu\text{A} < I_{C0}$, and consequently a load resistance $R_{\rm load} = 1\ \text{k}\Omega \gg R_N$ would provide an output voltage of 10 mV. On the one hand, to have a sizable output current, the load resistance is required to be much

smaller than the normal-state resistance of the transistor ($R_{\rm load} \ll R_N$). Yet, values of $R_{\rm load}$ on the order of kilohms are necessary to obtain significant output voltages (on the order of millivolt). As a consequence, transistors with high normal-state resistance are required. This can be achieved by use of structures with channels constituted of long metallic wires (a few micrometers) [13].

Figure 7(d) shows a schematic of the realization of NOT, AND, and OR logic gates with the electric-field-controlled-cryotron technology. The NOT gate is formed by the series of two constrictions: the first can be tuned by the input gate electrode (A), while the second is characterized by a critical current lower than $I_{\rm bias}$. When the input A is *low*, the current can pass through the first constriction without switching it, while the second constriction passes to the normal state. As a consequence, the current flows through the load resistance and the output signal is *high*. In contrast, when A is *high*, the first constriction switches to the normal state and the current does not flow in the device core. Therefore, the output signal is *low*. The AND and OR logic gates (see Fig. 7d) are realized by our placing two electric-field-controlled cryotrons in parallel; the difference between the two configurations resides in the magnitude of $I_{\rm bias}$ compared with the critical current of the single constriction: if $I_{\rm bias} > I_{CA} = I_{CB}$, the device behaves as an OR logic gate, while if $I_{\rm bias} < I_{CA} = I_{CB}$, the architecture works as an AND logic gate.

In this architecture the minimum switching energy for a single logic operation is given by $E_{\rm sw} \simeq LI_{\rm bias}^2$, where L is the device inductance [49]. In our devices $L \simeq 1$ pH gives $E_{\rm sw} \simeq 10^{-22}$ J for the switching of a single bit, which is some orders of magnitude lower than in single-flux quantum systems [52]. Furthermore, the switching time estimated from $\tau = L/R_N$ is on the order of 10^{-15} s, which corresponds to a switching frequency of 1000 THz. Finally, the electric-field-controlled-cryotron technology shows several interesting features for real circuits: strong gate/potential isolation (i.e., the gate impedance has been measured to range from 1 to 1000 TΩ depending on the dielectric material used [13,14]), low gate dissipation, and simple *monolithic* fabrication process, structure, and composition.

VIII. CONCLUSIONS

In conclusion, we describe a broad-range set of transport experiments performed on different fully metallic Dayem-bridge field-effect transistors and a thermodynamic model that is able to account for some phenomenological aspects of our findings.

The measurements of the critical current as a function of gate voltage highlight the suppression of I_C in a symmetric fashion with the polarity of V_G and the growth of a subgap dissipative component just above the full annihilation of the supercurrent. Furthermore, the normal-state resistance of our DB FET is completely insensitive to the electric field. All these results suggest that field-effect-induced charge accumulation/depletion is too small to be detected in our experimental conditions and cannot be the origin of the phenomenology presented. By independently controlling the voltage (V_{G1} and V_{G2}) applied to two gate electrodes placed at the opposite sides of the constriction, we demonstrate the independence of the effect of V_{G1} and V_{G2} on I_C. As a consequence, all these findings seem to suggest that the phenomena described occur at the metal surface and affect the superconductor over a few times the coherence length ξ.

The measurements of the Josephson current as a function of temperature show the transition from a ballistic constriction Kulik-Omelyanchuk behavior to a tunnellike Ambegaokar-Baratoff behavior with increasing gate voltage. This change of behavior is confirmed by our fitting the experimental data with a model describing the critical current of a generic Josephson junction. In particular, the effective transmission probability of the constriction extrapolated from the fits drops to zero for gate voltages reaching the critical value V_{GC} for the different device.

The zero-bias resistance measurements highlight the independence of the superconducting critical temperature and critical magnetic field (onset) on V_G and the growth of a subgap resistive component for gate voltages approaching V_{GC} (which is reflected in a widening of the superconducting transition with B). These results are in agreement with the I_C-versus-V_G measurements and suggest that the electric field induces the creation of an inhomogeneous superconductor–normal-metal state. The I_C-versus-B data show two main features: the plateau of the critical current with V_G widens with increasing out-of-plane magnetic field, while V_{GC} decreases with increasing B.

We present a phenomenological thermodynamic model that is able to account for some of the experimental observations: the electric-field-induced suppression of the supercurrent and the emergence of an inhomogeneous normal/superconducting state. The complete understanding of the impact of the electric field on superconductivity would benefit from a set of complementary experiments, such as probing the superconductor density of states through tunneling spectroscopy, investigating the phase rigidity in superconducting quantum-interference devices, examining the thermal transport in phase-biased Josephson junctions, and studying the kinetic inductance in superconducting resonators.

From an application point of view, this phenomenology paves the way to the realization of gate-tunable superconducting devices such as interferometers [37–39], photon detectors [40], coherent caloritronic systems [42–46], parametric amplifiers [41], gate-tunable metallic superconducting qubits [47,48], and superconducting classical electronics [49,50]. Finally, the use of higher-critical-temperature or higher-resistivity metallic

superconductors, such as vanadium and niobium, would boost the implementation of our technology in high-speed and low-dissipation superconducting electronics.

ACKNOWLEDGMENTS

The authors acknowledge the European Research Council under the European Union's Seventh Framework Programme (COMANCHE; European Research Council Grant No. 615187), the European Union under the Seventh Framework Programme (COHEAT; Research Executive Agency Grant No. 630925), and MIUR under the FIRB 2013 project Coca (Grant No. RBFR1379UX) for partial financial support. The work of G.D.S. and F.P. was partially funded by the Tuscany Region under the FARFAS 2014 project SCIADRO. The work of F.P. was partially supported by the Tuscany Government (Grant No. POR FSE 2014-2020) through the INFN-RT2 172800 project. A.B. acknowledges the CNR-CONICET cooperation program "Energy conversion in quantum nanoscale hybrid devices" and the Royal Society through the International Exchanges program for exchanges between the United Kingdom and Italy (Grant No. IES R3 170054).

[1] G. Bonfiglioli and R. Malvano, Modulation of conductivity by surface charges in metals, Phys. Rev. **101**, 1281 (1956).
[2] G. Bonfiglioli and R. Malvano, Surface states in metals, Phys. Rev. **115**, 330 (1959).
[3] A. Berman and H. J. Juretschke, Origin of the metallic field effect, Phys. Rev. B **11**, 2903 (1975).
[4] R. Glover and M. Sherrill, Changes in Superconducting Critical Temperature Produced by Electrostatic Charging, Phys. Rev. Lett. **5**, 248 (1960).
[5] G. Bonfiglioli, R. Malvano, and B. B. Goodman, Search for an effect of surface charging on the superconducting transition temperature of tin films, J. Appl. Phys. **33**, 2564 (1962).
[6] G. A. Ummarino, E. Piatti, D. Daghero, R. S. Gonnelli, I. Yu. Sklyadneva, E. V. Chulkov, and R. Heid, Proximity Eliashberg theory of electrostatic field-effect doping in superconducting films, Phys. Rev. B **96**, 064509 (2017).
[7] M. J. Panzer, C. R. Newman and C. D. Frisbie, Low-voltage operation of a pentacene field-effect transistor with a polymer electrolyte gate dielectric, Appl. Phys. Lett. **86**, 103503 (2005).
[8] A. S. Dhoot, J. D. Yuen, M. Heeney, I. McCulloch, D. Moses, and A. J. Heeger, Beyond the metal-insulator transition in polymer electrolyte gated polymer field-effect transistors, Proc. Natl. Acad. Sci. U. S. A. **103**, 11834 (2006).
[9] D. Daghero, F. Paolucci, A. Sola, M. Tortello, G. A. Ummarino, M. Agosto, R. S. Gonnelli, J. R. Nair, and C. Gerbaldi, Large Conductance Modulation of Gold Thin Films by Huge Charge Injection via Electrochemical Gating, Phys. Rev. Lett. **108**, 066807 (2012).
[10] M. Tortello, A. Sola, K. Sharda, F. Paolucci, J. R. Nair, C. Gerbaldi, D. Daghero, and R. S. Gonnelli, Huge field-effect surface charge injection and conductance modulation in metallic thin films by electrochemical gating, Appl. Surf. Sci. **269**, 17 (2013).
[11] D. Choi, R. Pradheesh, H. Kim, H. Im, Y. Chong, and D.-H. Chae, Electrical modulation of superconducting critical temperature in liquid-gated thin niobium films, Appl. Phys. Lett. **105**, 012601 (2014).
[12] E. Piatti, D. Daghero, G. A. Ummarino, F. Laviano, J. R. Nair, R. Cristiano, A. Casaburi, C. Portesi, A. Sola, and R. S. Gonnelli, Control of bulk superconductivity in a BCS superconductor by surface charge doping via electrochemical gating, Phys. Rev. B **95**, 140501 (2017).
[13] G. De Simoni, F. Paolucci, P. Solinas, E. Strambini, and F. Giazotto, Metallic supercurrent field-effect transistor, Nat. Nanotechnol. **13**, 802 (2018).
[14] F. Paolucci, G. De Simoni, P. Solinas, E. Strambini, and F. Giazotto, Ultra-efficient superconducting Dayem bridge field-effect transistor, Nano Lett. **18**, 4195 (2018).
[15] C. Varnava, Transistors go metal, Nat. Electron. **1**, 374 (2018).
[16] M. Jafari, H. Jammezhad, and L. Nazarzadeh, Electronic properties of titanium using density functional theory, IJST **A4**, 511 (2012).
[17] V. G. Zavodinky, Electronic states of nanostructured systems: Titanium and zirconia, Phys. Solid State **60**, 1903 (2018).
[18] T. D. Clark, R. J. Prance, and A. D. C. Grassie, Feasibility of hybrid Josephson field effect transistors, J. Appl. Phys. **51**, 2739 (1980).
[19] H. Takayanagi and T. Kawakami, Superconducting Proximity Effect in the Native Inversion Layer on InAs, Phys. Rev. Lett. **54**, 2449 (1985).
[20] T. Akazaki, H. Takayanagi, and J. Nitta, A Josephson field effect transistor using an InAs-inserted-channel $In_{0.52}Al_{0.48}As/In_{0.53}Ga_{0.47}As$ inverted modulation-doped structure, Appl. Phys. Lett. **68**, 418 (1996).
[21] V. Ambegaokar and B. I. Halperin, Voltage due to Thermal Noise in the DC Josephson Effect, Phys. Rev. Lett. **22**, 1364 (1969).
[22] A. F. Morpurgo, T. M. Klopwijk, and B. J. van Wees, Hot electron tunable supercurrent, Appl. Phys. Lett. **72**, 966 (1998).
[23] A. A. Golubov, M. Y. Kupriyanov, and E. Il'ichev, The current-phase relation in Josephson junctions, Rev. Mod. Phys. **76**, 412 (2004).
[24] I. O. Kulik and A. N. Omelyanchuk, Properties of superconducting microbridges in the pure limit, Sov. J. Low Temp. Phys. **3**, 945 (1977).
[25] V. Ambegaokar and A. Baratoff, Tunneling Between Superconductors, Phys. Rev. Lett. **10**, 486 (1963).
[26] R. C. Harwin, D. J. Goldie, and S. Withington, Modelling proximity effects in transition edge sensors to investigate the influence of lateral metal structures, Supercond. Sci. Technol. **30**, 084001 (2017).
[27] J. L. Levine, Dependence of Superconducting Energy Gap on Transport Current by the Method of Electron Tunneling, Phys. Rev. Lett. **15**, 154 (1965).
[28] Q. Zhang, G. Li, D. Rhodes, A. Kiswandhi, B. Zeng, J. Sun, T. Siegrist, M. D. Johannes, and L. Balicas,

Superconductivity with extremely large upper critical fields in $Nb_2Pd_{0.81}S_5$, Sci. Rep. **3**, 1446 (2013).
[29] P. G. De Gennes, *Superconductivity of Metals and Alloys,* (Westview Press, Boulder, 1999).
[30] M. Tinkham, *Introduction to Superconductivity,* (Courier Dover Publications, New York, 2012).
[31] J. A. Mydosh and H. Meissner, Dependence of the critical currents in superconducting films on applied magnetic field and temperature, Phys. Rev. **140**, A1568 (1965).
[32] R. E. Prange, Dielectric constant of a superconductor, Phys. Rev. **129**, 2495 (1963).
[33] J. Seiden, La constante diélectrique statique d'un supraconducteur, J. Phys. Fr. **27**, 561 (1966).
[34] M. Machida and T. Koyama, Friedel Oscillation in Charge Profile and Position Dependent Screening around a Superconducting Vortex Core, Phys. Rev. Lett. **90**, 077003 (2003).
[35] W. G. Jenks and L. R. Testardi, Electric-field penetration into superconducting and normal-state surfaces of $YBa_2Cu_3O_{7-x}$, Phys. Rev. B **48**, 12993 (1993).
[36] Z. Bao and Q. Sun, Ginzburg–Landau-type theory of spin superconductivity, Nat. Commun. **4**, 2951 (2013).
[37] J. Clarke and A. I. Bragisnki, *The SQUID Handbook* (Wiley, Weinheim, 2004).
[38] F. Giazotto, J. T. Peltonen, M. Meschke, and J. P. Pekola, Superconducting quantum interference proximity transistor, Nat. Phys. **6**, 254–259(2010).
[39] E. Strambini, S. D'Ambrosio, F. Vischi, F. S. Bergeret, Yu. V. Nazarov, and F. Giazotto, The ω-SQUIPT as a tool to phase-engineer Josephson topological materials, Nat. Nanotechnol. **11**, 1055–1059 (2016).
[40] G. N. Gol'tsman, O. Okunev, G. Chulkova, A. Semenov, K. Smirnov, B. Voronov, A. Dzardanov, and A. Lipatov, Picosecond Superconducting Single-Photon Optical Detector, Appl. Phys. Lett. **79**, 705 (2001).
[41] N. Bergeal, F. Schackert, M. Metcalfe, R. Vijay, V. E. Manucharyan, L. Frunzio, D. E. Prober, R. J. Schoelkopf, S. M. Girvin, and M. H. Devoret, Phase-preserving amplification near the quantum limit with a Josephson ring modulator, Nature **465**, 64 (2010).
[42] F. Giazotto and M. J. Martinez-Pérez, The Josephson heat interferometer, Nature **492**, 401–405 (2012).
[43] M. J. Martinez-Pérez, P. Solinas, and F. Giazotto, A quantum diffractor for thermal flux, Nat. Commun. **5**, 3579 (2014).
[44] A. Fornieri, C. Blanc, R. Bosisio, S. D'Ambrosio, and F. Giazotto, Nanoscale phase engineering of thermal transport with a Josephson heat modulator, Nat. Nanotechnol. **11**, 258–263 (2015).
[45] A. Fornieri, and F. Giazotto, Towards phase-coherent caloritronics in superconducting circuits, Nat. Nanotechnol. **12**, 944 (2017).
[46] M. J. Martinez-Pérez, P. Solinas, and F. Giazotto, Coherent caloritronics in Josephson-based nanocircuits, J. Low Temp. Phys. **175**, 813 (2014).
[47] T. W. Larsen, K. D. Petersson, F. Kuemmeth, T. S. Jespersen, P. Krogstrup J. Nygård, and C. M. Marcus, Semiconductor-Nanowire-Based Superconducting Qubit, Phys. Rev. Lett. **115**, 127001 (2015).
[48] G. de Lange, B. van Heck, A. Bruno, D. J. van Woerkom, A. Geresdi, S. R. Plissard, E. P. A. M. Bakkers, A. R. Akhmerov, and L. DiCarlo, Realization of Microwave Quantum Circuits Using Hybrid Superconducting-Semiconducting Nanowire Josephson Elements, Phys. Rev. Lett. **115**, 127002 (2015).
[49] A. N. McCaughan and K. K. Berggren, A superconducting-nanowire three-terminal electrothermal device, Nano Lett. **14**, 5784 (2014).
[50] Q.-Y. Zhao, A. N. McCaughan, A. E. Dane, K. K. Berggren, and T. Ortlepp, A nanocryotron comparator can connect single-flux-quantum circuits to conventional electronics, Supercond. Sci. Technol. **30**, 044002 (2017).
[51] K. K. Likharev, Superconductor digital electronics, Phys. C **482**, 6 (2012).
[52] M. H. Volkmann, A. Sahu, C. J. Fourie, and O. Mukhanov, Implementation of energy efficient single flux quantum digital circuits with sub-aJ/bit operation, Supercond. Sci. Technol. **26**, 015002 (2013).